

**Photoionization modeling of oxygen K absorption in the  
interstellar medium:  
the Chandra grating spectra of XTE J1817-330**

E. Gattuzz<sup>1</sup>, J. García<sup>2,3</sup>, C. Mendoza<sup>1,4</sup>, T.R. Kallman<sup>3</sup>, M. Witthoeft<sup>3</sup>, A. Lohfink<sup>2</sup>,

M.A. Bautista<sup>5</sup>, P. Palmeri<sup>6</sup>,

and

P. Quinet<sup>6,7</sup>

Received \_\_\_\_\_; accepted \_\_\_\_\_

---

<sup>1</sup>Centro de Física, Instituto Venezolano de Investigaciones Científicas (IVIC), PO Box 20632, Caracas 1020A, Venezuela

`egatuzz@ivic.gob.ve`, `claudio@ivic.gob.ve`

<sup>2</sup>Department of Astronomy and Maryland Astronomy Center for Theory and Computation, University of Maryland, College Park, MD 20742, USA

`javier@astro.umd.edu`, `alohfink@astro.umd.edu`

<sup>3</sup>NASA Goddard Space Flight Center, Greenbelt, MD 20771, USA

`timothy.r.kallman@nasa.gov`, `michael.c.witthoeft@nasa.gov`

<sup>4</sup>Centro Nacional de Cálculo Científico Universidad de Los Andes (CeCalCULA), Corporación Parque Tecnológico de Mérida, Mérida 5101, Venezuela

<sup>5</sup>Department of Physics, Western Michigan University, Kalamazoo, MI 49008, USA

`manuel.bautista@wmich.edu`

<sup>6</sup>Astrofysique et Spectroscopie, Université de Mons - UMONS, B-7000 Mons, Belgium

`palmeri@umons.ac.be`, `quinet@umons.ac.be`

<sup>7</sup>IPNAS, Sart Tilman B15, Université de Liège, B-4000 Liège, Belgium

## ABSTRACT

We present detailed analyses of oxygen K absorption in the interstellar medium (ISM) using four high-resolution *Chandra* spectra towards the X-ray low-mass binary XTE J1817-330. The 11–25 Å broadband is described with a simple absorption model that takes into account the pileup effect and results in an estimate of the hydrogen column density. The oxygen K-edge region (21–25 Å) is fitted with the physical **warmabs** model, which is based on a photoionization model grid generated with the XSTAR code with the most up-to-date atomic database. This approach allows a benchmark of the atomic data which involves wavelength shifts of both the K lines and photoionization cross sections in order to fit the observed spectra accurately. As a result we obtain: a column density of  $N_{\text{H}} = 1.38 \pm 0.01 \times 10^{21} \text{ cm}^{-2}$ ; ionization parameter of  $\log \xi = -2.70 \pm 0.023$ ; oxygen abundance of  $A_{\text{O}} = 0.689_{-0.010}^{+0.015}$ ; and ionization fractions of O I/O = 0.911, O II/O = 0.077, and O III/O = 0.012 that are in good agreement with previous studies. Since the oxygen abundance in **warmabs** is given relative to the solar standard of Grevesse & Sauval (1998), a rescaling with the revision by Asplund et al. (2009) yields  $A_{\text{O}} = 0.952_{-0.013}^{+0.020}$ , a value close to solar that reinforces the new standard. We identify several atomic absorption lines—K $\alpha$ , K $\beta$ , and K $\gamma$  in O I and O II; and K $\alpha$  in O III, O VI, and O VII—last two probably residing in the neighborhood of the source rather than in the ISM. This is the first firm detection of oxygen K resonances with principal quantum numbers  $n > 2$  associated to ISM cold absorption.

*Subject headings:* atomic data — atomic processes — ISM: general — X-rays: general — X-rays: binaries — stars: individual (XTE J1817-330)

## 1. Introduction

X-ray studies of interstellar absorption have the potential to provide information that is not accessible by other techniques. This includes the relative abundances of a wide range of ion stages of interstellar cosmic elements (e.g. oxygen) and the abundances relative to H and He of elements with atomic number  $Z \geq 6$ . X-ray absorption can also provide signatures of the binding of these elements in molecules or solids; the inner-shell electronic transitions are key diagnostics since the ionization state or chemical binding shifts the line energies by a predictable amount. The ongoing effort to explore and exploit this effect in interstellar studies involves accumulation of synthetic spectra for inner-shell absorption of ions and neutrals, based on both atomic calculation and laboratory experiment, in addition to testing them against available observed interstellar X-ray absorption spectra.

As part of the effort to accumulate the required atomic data, the atomic database of the XSTAR photoionization modeling code (Bautista & Kallman 2001) has been systematically improved in the past ten years in order to study the K lines and edges in the high-quality X-ray astronomical spectra obtained from the *Chandra* and *XMM-Newton* satellite-born observatories. This database includes K-vacancy levels, wavelengths,  $A$ -values, radiative and Auger widths and high-energy photoionization cross sections for complete isonuclear sequences with  $Z \leq 30$  (see Palmeri et al. 2012, and references therein).

With this new database it has been possible, for instance, to estimate the model efficiency of iron K-line emission and absorption in terms of the ionization parameter and density (Kallman et al. 2004). It has been shown that the centroid of the  $K\alpha$  unresolved transition array, the  $K\beta$  energy, and the ratio of the  $K\alpha_1$  to  $K\alpha_2$  components are useful diagnostics of the ionization parameter. It was also found that the many strongly damped resonances below the K-ionization thresholds lead to edge smearing, which can certainly hamper the astrophysical interpretation of the absorption features. A synthetic spectrum

has been modeled by Kallman et al. (2009) for the black-hole X-ray transient GRO J1655-40 which constrains the odd- $Z$  element abundances ( $11 \leq Z \leq 27$ ) and outflow parameters of the associated warm absorber. By analyzing the oxygen K-absorption structure in the interstellar medium (ISM) from the *XMM-Newton* spectrum of the low-mass X-ray binary Sco X-1, García et al. (2011) reproduced both the K edge and O I  $K\alpha$  absorption line, thus evaluating the impact of the atomic data on the interpretation of observations. In the present report we continue this work with a more stringent benchmark of the XSTAR atomic database, made possible by *Chandra* spectra of a low-mass binary displaying imprints of the ISM oxygen K absorption with higher resolution.

Juett et al. (2004) measured high-resolution spectra of the interstellar oxygen K-shell absorption edge from seven X-ray binaries—Cygnus X-1, Cygnus X-2, 4U 1636-53, 4U 1735-44, GX 9+9, 4U 1543-624, and 4U 1820-30—using the *Chandra* High Energy Transmission Grating Spectrometer (HETGS). The oxygen column density  $N_{\text{O}}$  was therein calculated using the optical depth at 21.7 Å and the cross section at this wavelength assuming the oxygen abundance from Wilms et al. (2000). With this value, the hydrogen column density  $N_{\text{H}}$  was then determined. The 1s-2p transitions of O II and O III were identified, finding ISM abundances for O II and O III relative to O I of  $\approx 0.1$  and  $\leq 0.1$ , respectively. This became the first estimate of the O II/O I and O III/O I abundance ratios in the ISM.

By observing the oxygen K-shell edge toward galaxy clusters, Baumgartner & Mushotzky (2006) showed that the ISM hydrogen X-ray column density was in close agreement with the 21 cm radio value for columns less than approximately  $0.5 \times 10^{21} \text{ cm}^{-2}$ . For higher column densities, the former was higher by as much as a factor of 2.5, indicating substantial absorption besides that due to neutral hydrogen (probably from clouds of molecular hydrogen). An average ISM oxygen abundance of 0.99 solar was found relative to the

photospheric value ( $8.66 \pm 0.05$ ) by Asplund et al. (2004) which implied a high gas to dust ratio.

Pinto et al. (2010) reported an spectral model suggesting that, along the line of sight towards an X-ray source (GS 1826-238), the ISM was more complex than just simple neutral gas. Their gas model consisted of three components: cold gas ( $T \approx 5.8-10 \times 10^3$  K); warm ionized gas ( $T \approx 1-6 \times 10^4$  K); and hot ionized gas ( $T \approx 2 \times 10^6$  K). It was also shown that the column densities  $N_{\text{H}}$  of these three components span two orders of magnitude, where the cold gas contributed  $\sim 90-95\%$ , the warm gas  $\sim 5-10\%$ , and the hot gas  $\sim 1\%$  to the total  $N_{\text{H}}^{\text{tot}}$ . Costantini et al. (2012) analyzed the ISM using the bright X-ray binary 4U 1820-30 source, concentrating on the mildly ionized cold gas where the model consisted of mildly ionized gas, dust, and mildly ionized outflowing gas. In the oxygen edge region, dust compounds were included which did not show features below  $23.7 \text{ \AA}$ . Finally, oxygen was found to be overabundant by a factor of 1.23 solar.

In order to model the oxygen K absorption features in the ISM with XSTAR, we need a *Chandra* spectrum with high counts. In the catalog of low-mass X-ray binaries by Liu et al. (2007), we found in XTE J1817-330 a suitable source with an average count number of  $\approx 8 \times 10^6$  counts/s. Discovered by the Rossi X-ray Timing Experiment (Remillard et al. 2006), XTE J1817-330 is a low-mass X-ray binary displaying a primary component which has an X-ray spectrum and variability behavior which are consistent with its identification as a black hole (Sala et al. 2007). Its location,  $l = 359.81$  and  $b = -7.99$  in Galactic coordinates, implies a line of sight in the Galactic center direction, a region that dominates the total mass of the Galaxy (Stasińska et al. 2012) providing a good opportunity to study the ISM absorption features. This source has been observed in different spectral ranges, namely the optical (Torres et al. 2006), near infrared (D’Avanzo et al. 2006), radio (Rupen et al. 2006), and X-ray (Roy et al. 2011). Sala et al. (2007) fitted its X-ray

spectrum finding an absorbing hydrogen column of  $1.55 \times 10^{21} \text{ cm}^{-2}$  and identifying the following oxygen absorption lines: O I  $K\alpha$ (23.52 Å); O II  $K\alpha$ (23.35 Å); O III  $K\alpha$ (23.13 Å); O I  $K\beta$ (22.91 Å); and O VII  $K\beta$ (21.60 Å). Gierliński et al. (2009) estimated a hydrogen column density of  $N_{\text{H}} = 1.08 \pm 0.05 \times 10^{21} \text{ cm}^{-2}$ , and Roy et al. (2011) investigated the timing characteristics in the spectra using a column of  $N_{\text{H}} = 1.2 \times 10^{21} \text{ cm}^{-2}$ .

The outline of the present report is as follows. In Section 2, we describe the XSTAR `warmabs` physical model which is used to obtain the final spectrum fits, in particular the details concerning its atomic database. The data reduction aspects of the observations, e.g. the pileup effect, are reviewed in Section 3 while the results of the broadband fits and resolved absorption features are given in Sections 4–5. Section 6 is dedicated to comparisons of the hydrogen column density that allow an estimate of its reliability. Section 7 describes the oxygen column densities derived from our fits. Finally, a discussion and conclusions are presented in Section 8.

## 2. XSTAR/warmabs

XSTAR<sup>1</sup> is a code package designed to determine the physical conditions in partially ionized gases. It calculates the temperature, ionization, excitation, absorption, and emission due to neutral and all ionized species of elements with atomic number  $Z \leq 30$ . As many relevant physical processes as possible are taken into account, assuming a time stationary balance among them and a Maxwellian electron velocity distribution. Important processes for many problems relevant to X-ray astronomy include photoionization, electron impact collisional ionization and excitation, and radiative and dielectronic recombination. More complete descriptions of XSTAR and its atomic database are given by Kallman & Bautista

---

<sup>1</sup><http://heasarc.nasa.gov/lheasoft/xstar/xstar.html>

(2001) and Bautista & Kallman (2001). In this work we employ the `warmabs` utility which allows for the calculation of XSTAR models within the widely used X-ray spectral fitting package XSPEC<sup>2</sup>. It utilizes precalculated tabulations of the ion fractions and level populations in order to calculate synthetic emission and transmission spectra. It assumes that the gas responsible for emission or absorption has a uniform ionization and temperature throughout, although it is possible to superimpose two or more components and simulate a non-uniform situation.

## 2.1. Atomic data

The K photoabsorption data sets for oxygen ions with electron numbers  $2 \leq N \leq 8$  contained in the XSTAR atomic database were generated by García et al. (2005). Energies for both valence and K-vacancy fine-structure levels, transition wavelengths,  $gf$ -values, and radiative and Auger widths were computed with the atomic structure packages AUTOSTRUCTURE (Eissner et al. 1974; Badnell 1986, 1997) and HFR (Cowan 1981). Electron correlation effects were taken into account by means of configuration-interaction expansions within the  $n \leq 3$  complexes, and relativistic corrections were included with a Breit–Pauli Hamiltonian. The accuracy of the theoretical level energies and wavelengths does not generally match that attained in experiments (see Table 1), and the scanty availability of measurements for the K shell of O ions with  $N > 3$  limits the implementation of term-energy corrections and wavelength shifts that can be introduced in order to compensate for the theoretical shortcomings. Furthermore, as also shown in Table 1, experimental misassignments, such as that quoted by Gu et al. (2005) for O VI, are not uncommon. (The discrepancy in O III is believed to be a typo.)

---

<sup>2</sup><http://heasarc.gsfc.nasa.gov/xanadu/xspec/>

High-energy photoionization cross sections in the K-edge region for oxygen ions were obtained by García et al. (2005) with BPRM, the Breit–Pauli  $R$ -matrix suite of codes (Scott & Burke 1980; Scott & Taylor 1982; Berrington et al. 1987; Seaton 1987). A conspicuous effect in the resonance structure of these cross sections that must be treated in detail is Auger damping. It is the result of the dominant spectator KLL Auger decay channels of a photoexcited K-vacancy state, say,

$$[1s]2p^\mu np \rightarrow 2p^{\mu-2}np + e^- \quad (1)$$

$$\rightarrow [2s]2p^{\mu-1}np + e^- \quad (2)$$

$$\rightarrow [2s]^2 2p^\mu np + e^- \quad (3)$$

over the participator Auger  $KLn$  channels

$$[1s]2p^\mu np \rightarrow 2p^{\mu-1} + e^- \quad (4)$$

$$\rightarrow [2s]2p^\mu + e^- , \quad (5)$$

which leads to edge smearing by resonances with symmetric profiles of nearly constant width. They are handled within the  $R$ -matrix package by means of an optical potential (Gorczyca & Robicheaux 1999; Gorczyca & McLaughlin 2000). Again, the accuracy of the resonance energy positions is limited by the absence of measurements which would enable empirical adjustments of the many K-vacancy target thresholds (i.e. the series limits) in the close-coupling expansion.

### 3. Observations and data reduction

In Table 2 we list the specifications of the four observations of XTE J1817-330 obtained by *Chandra* using the High Energy Transmission Grating Spectrometer (HETGS) in combination with the Advanced CCD Imaging Spectrometer (ACIS). The oxygen edge is

accessible with the HETGS exclusively via the Medium Energy Gratings (MEG). Given the large flux of this source ( $F = 1350 \mu\text{J}$ , integrated in the 2–10 keV energy range), these observations were taken in continuous clocking mode which significantly increases the temporal resolution in order to minimize the *pileup* effect (Cackett et al. 2008). The pileup is an inherent feature of CCD detectors, such as those of the ACIS instrument, which occurs when two or more photons are detected as a single event possibly causing a deformation in the level and shape of the continuum (Miller et al. 2006b). It is stronger in the MEG than in the HEG due to the lower dispersion and higher effective area of the former<sup>3</sup>. Although the pileup is usually not an issue near the oxygen edge, it may be for the continuum which is used to establish the hydrogen column density by fitting the 11–25 Å interval; hence, we consider the pileup effect in this range by applying the correction model `simple_gpile2.sl` (Hanke et al. 2009) before spectral fitting. Among the most popular computer packages for fitting X-ray data are XSPEC and ISIS, and we have used the latter (version 1.6.2<sup>4</sup>) to include the pileup model.

Even though the spatial resolution is reduced to one dimension when the continuous clocking mode is used, there is essentially no difference with the timed exposure mode in the background extraction or in the data reduction process. Hence, we have reduced the data sets using the standard CIAO threads<sup>5</sup>. In some cases, the zero-order data were not telemetered; for these observations the zero-order position was then estimated by finding the intersection of the grating arms using the `findzo` algorithm<sup>6</sup>.

Figure 1 shows the light curves of the four observations ObsID 6615, 6616, 6617, and

---

<sup>3</sup>[http://cxc.harvard.edu/ciao/ahelp/acis\\_pileup.html](http://cxc.harvard.edu/ciao/ahelp/acis_pileup.html)

<sup>4</sup><http://space.mit.edu/cxc/isis/>

<sup>5</sup><http://cxc.harvard.edu/ciao4.4/threads/gspec.html>

<sup>6</sup><http://space.mit.edu/cxc/analysis/findzo/>

6618 in units of counts/s. It may be seen that the average counts/s is approximately constant for all, and therefore, we use the averaged spectra for this work. We have carried out the following spectral fitting procedure: firstly, each spectrum was rebinned with a 0.1 Å bin in order to fit the continuum in the 11–25 Å wavelength range so as to find the hydrogen column density using the `TBnew` model; then, the default spectral resolution was restored, and the oxygen edge region (21–24 Å) was analyzed with the `warmabs` model freezing the column density at the value obtained in the preceding step.

#### 4. Broadband fit

Following Yao & Wang (2006), we rebinned each spectrum with a 0.1 Å bin size throughout the spectral range to decrease the number of absorption lines and improve the broadband fit. We fitted the four observations simultaneously in the interval 11–25 Å using the `simplegpile2(TBnew(powerlaw))` model, where `simplegpile2` is a convolution model to account for pileup effects and `TBnew` is an X-ray absorption model that includes abundances for elements from H to Ni (Wilms et al. 2000). Also we added Gaussians to fit the remaining absorption lines after rebinning. We used abundances specified in Wilms et al. (2000) and cross sections by Verner et al. (1996). The O, Ne, and Fe abundances were handled as free parameters, and for the analysis  $\chi^2$  statistics was employed. We fixed the absorption parameters in all the observations, and varied the power-law, pileup, and Gaussian parameters for each case.

Figure 2 shows the fit in the interval 11–25 Å using the `simplegpile2(TBnew(powerlaw))` model. Although the fit is carried out simultaneously for the four observations, they are plotted separately to improve clarity. Panels (a), (b), (c), and (d) correspond to observations ObsID 6615, 6616, 6617, and 6618, respectively (see Table 2). In each panel, black data points correspond to the observation while the solid red lines represent the

best-fit model for each case, and the base plots show the fit residuals in units of  $\chi^2$ . In each spectrum the K edges of Ne and O are respectively located at  $\approx 14.3 \text{ \AA}$  and  $\approx 23.2 \text{ \AA}$ . The O I and O II 1s–2p absorption lines at  $23.5 \text{ \AA}$  and  $23.35 \text{ \AA}$  are also clearly observed. We improved the fit by including Gaussians to model the outstanding absorption lines: Ne IX  $K\alpha$  ( $\approx 13.43 \text{ \AA}$ ); Ne III  $K\alpha$  ( $\approx 14.50 \text{ \AA}$ ); Ne II  $K\alpha$  ( $\approx 14.60 \text{ \AA}$ ); O VIII  $Ly\alpha$  ( $\approx 18.95 \text{ \AA}$ ); O VII  $K\alpha$  ( $\approx 21.58 \text{ \AA}$ ); and O II  $K\alpha$  ( $\approx 23.34 \text{ \AA}$ ). Residuals indicate that the model fits the data satisfactorily with deviations near the Ne edge ( $\approx 14.3 \text{ \AA}$ ) due to background (i.e. clocking the whole chip) or an unaccounted hot pixel. We also find high residuals in the oxygen absorption region; in particular, the O I  $K\alpha$  and O II  $K\alpha$  are not well modeled.

Fit results for the individual free abundances, column density, power law, and pileup are presented in Table 3. The fit statistics give a reduced chi-square of  $\chi^2 = 1.208$ . Differences in the power-law parameters are due to the count numbers in each observation. We obtain abundances for O, Ne, and Fe higher than solar (Wilms et al. 2000), especially for Ne (factor of 2), and a column density of  $N_{\text{H}} = 1.66_{-0.04}^{+0.03} \times 10^{21} \text{ cm}^{-2}$  which is somewhat larger than those estimated in other spectral fits and by measurements of the 21 cm line. This will be further discussed in Section 6.

The nonlinear pileup convolution model `simple_gpile2.sl` exponentially reduces the predicted count rate  $R_j(\lambda)$  (in units of counts/s/ $\text{\AA}$ ) according to

$$R(\lambda) = R(\lambda) \exp(-\beta R_{\text{tot}}(\lambda)) \quad (6)$$

where  $R_{\text{tot}}(\lambda)$  is the total spectral count rate and  $\beta$  is treated as a fit parameter. The model is only applicable to first order grating spectra although it employs information from the second and third order grating spectra<sup>7</sup>. With this model we obtained an average  $\beta = 0.050$  according to which the spectra have a pileup degree greater than 25% for  $14 \leq \lambda \leq 16 \text{ \AA}$

---

<sup>7</sup>[http://cxc.harvard.edu/ciao/ahelp/acis\\_pileup.html](http://cxc.harvard.edu/ciao/ahelp/acis_pileup.html)

with the highest value of  $p = 42\%$  at  $\approx 14.3 \text{ \AA}$  for the observation with the largest number of counts (ObsID 6615). This value shows the need to include the pileup effect in the 11–25  $\text{\AA}$  region to obtain a good fit. However, for all the observations, we have a pileup degree lower than 5% in the 21–24  $\text{\AA}$  wavelength range which corresponds to the oxygen absorption region and, therefore, its effects were ignored.

## 5. Absorption features

In order to identify all the absorption features present in the 21–25  $\text{\AA}$  wavelength region, we first applied a functional model consisting of a power law for the continuum and Gaussian profiles to describe the absorption lines. Figure 3 shows the spectral fit of the four *Chandra* MEG observations of XTE J1817-330 in the oxygen absorption region. Although shown in separate panels for clarity, the fit was performed simultaneously for the four observations. Nevertheless, the power-law parameters (photon index and normalization) are allowed to vary independently for each data set. Several absorption features are clearly observed, the most outstanding being the O I and O II  $K\alpha$  lines. The base plot in each panel shows in units of  $\chi^2$  the fit residuals as a histogram. High residuals are found around 24.8  $\text{\AA}$ , and the model underestimates the number of photons around 23.2  $\text{\AA}$ .

Table 4 shows a list of the lines obtained with the functional fit including the centroid wavelengths derived from the Gaussian profile parameters. It also lists the wavelengths for the lines measured by Sala et al. (2007). Note that our wavelengths are within the error bars of the values reported by these authors, which are much larger given the lower spectral resolution of the *XMM-Newton* instruments. We obtain a reduced chi-square of  $\chi^2 = 1.434$ . The O I  $K\alpha$  is found at  $23.502 \pm 0.001 \text{ \AA}$  which has been previously declared of ISM origin (Sala et al. 2007). Furthermore, we have also detected four other O I absorption lines corresponding to resonances with higher principal quantum number  $n$ :

two pairs of  $K\beta$  ( $n = 3$ ) and  $K\gamma$  ( $n = 4$ ) resonances associated to the  $^4P$  and  $^2P$  K-hole core states. These are found at  $22.884 \pm 0.004 \text{ \AA}$ ,  $22.790 \pm 0.001 \text{ \AA}$ ,  $22.686 \pm 0.004 \text{ \AA}$ , and  $22.609 \pm 0.007 \text{ \AA}$ , respectively. In this set, only the first  $K\beta$  (belonging to the  $^4P$  core state) has been previously detected at  $22.91 \pm 0.03 \text{ \AA}$  in the *XMM-Newton* observation analyzed by Sala et al. (2007). This is then the first firm detection of oxygen K resonances with  $n > 2$  associated to ISM cold absorption.

The line at  $23.358 \pm 0.002 \text{ \AA}$  is also of ISM origin (Juett et al. 2004) and corresponds to O II  $K\alpha$ . As in the case of O I, resonances with  $n > 2$  were also detected for O II. These were found at  $22.280 \pm 0.003 \text{ \AA}$  and  $22.101 \pm 0.005 \text{ \AA}$  corresponding to  $K\beta$  and  $K\gamma$ , respectively. Although the O III  $K\alpha$  resonance is a triplet, only two absorption features were detected at  $23.104 \pm 0.005 \text{ \AA}$  and  $23.054 \pm 0.001 \text{ \AA}$  while Sala et al. (2007) only found one line at  $23.13 \pm 0.09 \text{ \AA}$  identified as O III  $K\alpha$ . Finally, we have also located  $K\alpha$  transitions for both O VI ( $22.022 \pm 0.003 \text{ \AA}$ ) and O VII ( $21.589 \pm 0.003 \text{ \AA}$ ), from which only the strongest of the two (O VII) was reported by Sala et al. (2007) at  $21.609 \pm 0.06 \text{ \AA}$ .

The functional fit described above illustrates the complexity of oxygen K absorption. There are (at least) two different regimes: a cold component of mostly neutral gas and a hot component with highly ionized gas. Previous studies have suggested a multiple-phase ISM; however, it is not clear if the two high-ionization lines from O VI and O VII are intrinsic to the source or in fact arise in the ISM. Thus we direct our study to the cold phase. Furthermore, since cold absorption is not exclusively due to neutral oxygen, this means that a model such as `TBnew` will not completely represent the observed features. We have then simultaneously fitted the four exposures in the 21–25  $\text{\AA}$  wavelength range using the `powerlaw*warmabs` physical model. The advantage of using `warmabs` is that it contains the most recent atomic data for all the ions in the oxygen isonuclear sequence, thus enabling the fit of all the absorption lines from O I, O II, and O III. While implementing this model,

the column density is held fixed at the value obtained in the broadband simultaneous fit ( $N_{\text{H}} = 1.66 \times 10^{21} \text{ cm}^{-2}$ ). The ionization parameter and the oxygen abundance are treated as free parameters but the same for all observations, while the abundances of all the other chemical elements are held fixed at their solar values. The quantities describing the power law (photon index and normalization) are also taken as free parameters but independently for each observation.

Figure 4 shows the results of this fit. As before, we present for clarity the spectra with the best-fit model in separate panels although the fit is performed simultaneously. Since most of the relevant absorption features in the spectra are due to neutral, singly, and doubly ionized O ions, the ionization parameter that describes the fit tends to be somewhat low:  $\log \xi = -2.729$ . In this case, the `warmabs` model does not show any absorption due to O VII; therefore, this line is still represented with a Gaussian profile. We have found large residuals around most of the oxygen absorption features, the most prominent being around the O I and O II  $K\alpha$  lines. The fit statistics gives a poor reduced chi-square of  $\chi^2 = 1.769$  which forced us to revise the atomic database.

A close examination of the resonance positions from the photoabsorption cross sections used in `warmabs` in comparison with those obtained from the spectral fits with Gaussian profiles reveals the inaccuracies of the atomic data. Figure 5a shows with solid colored lines the atomic cross sections used in `warmabs` for O I, O II, and O III (García et al. 2005). Vertical dashed lines are placed at the positions of the absorption features found with the functional fit described above (see Table 4). The comparison shows that not only the positions of the O I and O II  $K\alpha$  resonances are displaced with respect to the observed data but also those with  $n > 2$ . The solid black line represents the experimental O I photoabsorption cross section measured by Stolte et al. (1997) (unfortunately, there are no laboratory measurements available for the other species) which displays a similar

wavelength shift with respect to the observed resonance positions. This wavelength offset has been previously discussed by Juett et al. (2004) based on the  $K\alpha$  position observed in the *Chandra* spectra from several sources, all of which match the position we have found using Gaussian profiles. For O I, the comparison of the theoretical cross section with the laboratory measurement shows that, except the  $K\alpha$  peak, all the other resonances agree very well. This implies that the relative position of the  $K\alpha$  with respect to the other resonances also needs to be adjusted. This is also the case for O II since the wavelength difference of the theoretical and observed  $K\alpha$  positions is not the same as those for the rest of the resonances of the same ion. Consequently, we have decided on the one hand to adjust the positions of the  $K\alpha$  resonances (which are treated as lines in `warmabs`), and on the other, to shift the whole cross sections for both species so as to obtain the best possible agreement with the observed lines. The new positions for the O I and O II  $K\alpha$  lines are 23.502 Å and 23.343 Å while the cross sections were shifted towards shorter wavelengths by 0.033 Å and 0.079 Å, respectively. No correction was applied to the O III curve since the observed lines are weaker, in addition to the fact that in this case the  $K\alpha$  resonance is a triplet. Figure 5b shows the atomic absorption cross sections after the wavelength corrections are applied. In other words, the *Chandra* observed line positions suggest not only that the theoretical resonance positions from García et al. (2005) must be adjusted, but also that the wavelength scale of the only available experiment for O I (Stolte et al. 1997) needs to be shifted by 33 mÅ.

Possible effects due to the instrument wavelength calibration, model uncertainties, and Doppler shifts due to motion of the gas in the ISM are important for accurate line identification. The instrumental resolution for the first-order spectra from MEG is  $\Delta\lambda \sim 23$  mÅ, which is better than the largest shift required for our theoretical cross sections (33 mÅ). In fact, according to García et al. (2005), the uncertainties in the theoretical cross sections for O ions with electron occupancies  $N \leq 4$  were estimated to be

$\sim 50 \text{ m}\text{\AA}$ , comparable with the wavelength uncertainties in the laboratory measurements of Stolte et al. (1997). Assuming a velocity dispersion for the ISM of  $\leq 200 \text{ km s}^{-1}$  (Juett et al. 2004), the largest wavelength shift due to Doppler effects for the O I  $K\alpha$  is  $\Delta\lambda = 14 \text{ m}\text{\AA}$ , which is smaller than the instrumental resolution. Hence, we can safely ignore the effects of ISM gas motion in the light of sight.

Figure 6 shows the fit results with **warmabs** after the theoretical line positions have been corrected, where the residuals are now significantly reduced and more evenly distributed. This is reflected in better fit statistics (reduced  $\chi^2 = 1.245$ ) and a well-constrained ionization parameter ( $\log \xi = -2.699 \pm 0.023$ ) which is consistent with the low-ionization oxygen lines observed. As before, the O VII  $K\alpha$  resonance at  $21.589 \text{ \AA}$  is not well represented with this model and must be fitted with a Gaussian profile. We have also noticed that the absorption feature at  $22.022 \text{ \AA}$  is not entirely due to the O III  $K\delta$  resonance and is thus fitted with a Gaussian profile, confirming a blend of both O III  $K\delta$  and O VI  $K\alpha$ . In this final analysis, we also treated the column density value as free parameter in order to increase the accuracy of the fit. We find a column density of  $N_{\text{H}} = 1.38 \pm 0.1 \times 10^{21} \text{ cm}^{-2}$  that is lower than the value previously mentioned in connection with the broadband fit (see Section 4). The oxygen abundance obtained with the **warmabs** model is  $A_{\text{O}} = 0.689_{-0.010}^{+0.015}$  relative to solar, also lower than the value for the best fit with **TBnew** ( $A_{\text{O}} = 1.178 \pm 0.22$ ). All the best-fit parameters of the **warmabs** are summarized in Table 5.

## 6. Hydrogen column density

Table 6 shows a comparison of the hydrogen column density obtained in this work with previous estimates including measurements using the 21 cm line. By means of the simultaneous broadband fit described in Section 4, we have obtained a column density of  $N_{\text{H}} = 1.66_{-0.04}^{+0.03} \times 10^{21} \text{ cm}^{-2}$  which is somewhat larger than those quoted in previous spectral

fits. Miller et al. (2006a) reported a hydrogen column density of  $N_{\text{H}} = 8.8\text{--}9.7 \times 10^{20} \text{ cm}^{-2}$  using a 50 ksec *Chandra* spectrum, a value smaller than those obtained from Galactic H I surveys, e.g.  $1.58 \times 10^{21} \text{ cm}^{-2}$  (Dickey & Lockman 1990) and  $1.39 \times 10^{21} \text{ cm}^{-2}$  (Kalberla et al. 2005). Using the equivalent widths of several interstellar bands in the optical spectrum, Torres et al. (2006) found the column density to be in the range  $N_{\text{H}} = 1\text{--}3 \times 10^{21} \text{ cm}^{-2}$ . Moreover, both Rykoff et al. (2007) and Gierliński et al. (2008) gathered acceptable fits of several *Swift* XRT spectra with a fixed Galactic column density of  $N_{\text{H}} = 1.2 \times 10^{21} \text{ cm}^{-2}$ . Gierliński et al. (2009) used the same XRT spectra combined with data from UVOT (The Ultraviolet and Optical Telescope) to derive a column density of  $N_{\text{H}} = 1.08 \pm 0.05 \times 10^{21} \text{ cm}^{-2}$  from broadband spectral fits.

The agreement between **TBnew** and Sala et al. (2007) is around 7% despite the fact that their fits include data from *XMM-Newton* EPIC-Pn (0.6–10.0 keV), RGS1 (0.3–2.0 keV), and OM covering a much wider energy range; furthermore, they model the foreground absorption with **TBabs**, an older version of **TBnew** (Wilms et al. 2000). On the other hand, the present fits of the oxygen K region (21–25 Å) with the **warmabs** physical model yield a lower column density ( $N_{\text{H}} = 1.38 \pm 0.1 \times 10^{21} \text{ cm}^{-2}$ ) than that derived from our broadband fit and **TBnew**. This discrepancy is expected due to the different atomic data sets involved, particularly since **TBnew** only includes the photoabsorption cross section for neutral oxygen. Taking into account the scatter of the previous column densities in the literature and the fact that we have adequately modeled the absorption features from O I, O II, and O III, we would expect the value derived from **warmabs** to be more reliable than that from **TBnew**.

## 7. Oxygen column density

In order to derive the O column density along the line of sight of XTE J1817-330, we have calculated the curve of growth for each of the oxygen  $K\alpha$  transitions using the

atomic data from García et al. (2005), and equivalent widths (EWs) have been obtained using the functional fit described in Section 5. Table 7 shows a comparison between the present  $K\alpha$  EWs for O I, O II, O III, O VI, and O VII and those by Sala et al. (2007) for XTE J1817-330. EWs listed in Juett et al. (2004) for seven other sources are also included as well as those by Yao et al. (2009) for Cygnus X-2. For O I  $K\alpha$ , our EW ( $51 \pm 5$  mÅ) is around the lower limits of Sala et al. (2007) and Juett et al. (2004), and for O II  $K\alpha$ , the present value of  $52 \pm 5$  mÅ is within the range that Juett et al. (2004) associated with the ISM. However, we find the  $K\alpha$  lines in both O I and O II to be saturated which could influence our derived EWs. Furthermore, the  $K\alpha$  EWs in O III, O VI, and O VII are in good agreement with the values obtained by Juett et al. (2004), Sala et al. (2007), and Yao et al. (2009).

Table 8 shows a comparison of the oxygen column densities obtained from the EWs and the **warmabs** model fit. As previously mentioned in Section 5, for the ionization parameter found in our best **warmabs** fit, only O I, O II, and O III are included in the model. As a reference, we have also included the oxygen column density for O VI from Savage et al. (2003), obtained from FUSE data for four sources located near the same Galactic latitude as XTE J1817-330. The curve-of-growth values for O I, O II, and O III result in a total column density of  $N_{\text{O}} = N_{\text{OI}} + N_{\text{OII}} + N_{\text{OIII}} = 5.71 \times 10^{17} \text{ cm}^{-2}$ , in relatively good agreement with that derived from the ionic fractions in the **warmabs** fit, namely  $N_{\text{O}} = 6.41 \times 10^{17} \text{ cm}^{-2}$ . However, the ratios O I/O II are significantly different: 1.4 and 11.9, respectively. Due to line saturation, the measured EWs are likely to be underestimated, in particular for the O I  $K\alpha$  line. This leads to a higher uncertainty in the column and ion fractions estimated from the EW measurements. On the other hand, since the parameters in the **warmabs** fit are constrained by all the lines as well as the K edge, we are more confident about their reliability. In the case of the O VI and O VII  $K\alpha$  transitions, because the EWs are on the flat section of the curve of growth, they strongly depends on velocity dispersion. For

O VI  $K\alpha$ , the oxygen column density spans from  $N_{\text{OVI}} = 71.12 \pm 29.15 \times 10^{15} \text{ cm}^{-2}$  to  $N_{\text{OVI}} = 5.06 \pm 2.53 \times 10^{15} \text{ cm}^{-2}$  when using dispersion velocities of  $v = 20 \text{ km s}^{-1}$  and  $v = 200 \text{ km s}^{-1}$ , respectively. The smallest value is still about one order of magnitude larger than that reported by Savage et al. (2003), making difficult to constrain the the velocity dispersion. Also, no real improvement is achieved by considering larger dispersions, as the column density is reduced very little once the velocities are larger than  $200 \text{ km s}^{-1}$ . This may be an indication that the observed O VI line is likely to originate from the neighborhood of XTE J1817-330 rather than from the ISM. In the case of O VII, the oxygen column density varies from  $N_{\text{OVII}} = 4.48 \pm 1.84 \times 10^{18} \text{ cm}^{-2}$  ( $v = 20 \text{ km s}^{-1}$ ) to  $N_{\text{OVII}} = 4.5 \pm 1.8 \times 10^{16} \text{ cm}^{-2}$  ( $v = 200 \text{ km s}^{-1}$ ).

## 8. Discussion and conclusions

There are several interesting conclusions emerging from this work that configure a set of useful guidelines in the analysis of ISM absorption features in *Chandra* and *XMM-Newton* spectra. In order to resolve such spectral signatures, bright sources with high count rates are desirable. In the present XTE J1817-330 study case, we were fortunate to find four good quality spectra that were fitted simultaneously so as to obtain improved statistics. However, it was realized that the pileup effect must be taken into account in order to obtain reasonably reliable hydrogen column densities. This effect was treated adequately with the nonlinear pileup convolution model `simple_gpiled2.sl`, whereby the pileup was estimated by fitting the continuum to be on average around 25%. The resulting hydrogen column density is  $N_{\text{H}} = 1.66_{-0.04}^{+0.03} \times 10^{21} \text{ cm}^{-2}$ , which is somewhat ( $\lesssim 7\%$ ) higher than those by Kalberla et al. (2005) and Sala et al. (2007), the former obtained from 21 cm data.

The absorption features in the oxygen region (21–25 Å) were first picked up with a functional model (power law and Gaussian profiles) which yielded  $K\alpha$  lines of O I, O II,

O III, O VI, and O VII previously observed by Sala et al. (2007), but for the first time, also K resonances of O I and O II with principal quantum number  $n > 2$ . These line identifications at least confirm a two-phase plasma with both neutral (mostly) and highly ionized components. In the present work we have been mainly concerned with the former. In this respect, since neutral oxygen is not the sole charge state responsible for the cold oxygen absorption, the four exposures are then simultaneously fitted with a representative physical model referred to as `warmabs`, which contains the atomic data for the oxygen isonuclear sequence computed by García et al. (2005). In this step, the hydrogen column density is held fixed at the previously determined value of  $N_{\text{H}} = 1.66 \times 10^{21} \text{ cm}^{-2}$  while the ionization parameters and oxygen abundance are treated as free parameters. A detailed comparison of this model with observations brings forth the inaccuracies of the atomic data, which led us to introduce wavelengths shifts in both the  $K\alpha$  line positions and photoabsorption cross sections of O I and O II.

The scope of this corrective procedure is severely limited by the general poor availability of laboratory data for the oxygen inner-shell, but it certainly leads to improved fits and statistics; in particular, to a well-constrained ionization parameter of  $\log \xi = -2.699 \pm 0.023$  consistent with the absorption lines observed. In order to further improve the fit, the column density is allowed to vary resulting in a more reliable value ( $N_{\text{H}} = 1.38 \pm 0.1 \times 10^{21} \text{ cm}^{-2}$ ) which is within 13% of previous estimates (Kalberla et al. 2005; Sala et al. 2007). Furthermore, the fit yields an oxygen abundance of  $A_{\text{O}} = 0.689_{-0.010}^{+0.015}$  and ionization fractions of O I/O = 0.911, O II/O = 0.077 and O III/O = 0.012. Regarding the oxygen abundance, it may be clarified that the quoted value is given relative to the solar standard ( $8.83 \pm 0.06$ ) of Grevesse & Sauval (1998). If it is rescaled to the recently revised standard by Asplund et al. (2009) of  $8.69 \pm 0.05$ , then an ISM abundance ( $A_{\text{O}} = 0.952_{-0.013}^{+0.020}$ ) close to solar is obtained that is in excellent accord with the averaged value by Baumgartner & Mushotzky (2006), and can be included as further support for the

solar abundance revision. Moreover, our ionization fractions are in good agreement with those found by Juett et al. (2004) of  $\text{O II}/\text{O I} \approx 0.1$  and  $\text{O III}/\text{O I} \leq 0.1$ .

The functional fit allows us to derive oxygen column densities by means of a curve of growth method using the EWs for each of the observed  $\text{K}\alpha$  absorption lines, which can then be compared with the values obtained from the `warmabs` fit. Even though we find by both methods a relatively consistent total column density ( $5.71 \times 10^{17} \text{ cm}^{-2}$  in the curve of growth and  $N = 6.41 \times 10^{17} \text{ cm}^{-2}$  in the `warmabs` model fit), the  $\text{O I}/\text{O II}$  ratio for the  $\text{K}\alpha$  lines is significantly lower (an order of magnitude) in the former. This is attributed to the high saturation level in both lines which leads to underestimates of the measured EWs, and we are therefore confident that the results from the `warmabs` model fit are more reliable. In the case of  $\text{O VI}$ , the width of the line strongly depends on the velocity dispersion of the gas. For the velocity dispersion values expected in the ISM ( $v \sim 20 - 200 \text{ km s}^{-1}$ ), the EWs obtained with our functional fit yield oxygen column densities far above from the FUSE values by Savage et al. (2003). This may be an indication that the  $\text{O VI}$  observed absorption in the XTE J1817-330 spectra is bound to occur near the source rather than in the ISM.

We find acceptable fits to the observed oxygen K-edge spectrum with a model consisting of atomic oxygen ions if the energies are slightly adjusted. However, it is also of great interest to detect or set limits on features due to other phases of interstellar oxygen and other elements, namely molecules or solids (dust). It is expected that these phases comprise a significant fraction of the total oxygen column in the ISM. Evidence for this includes observed depletions of atomic oxygen along many lines of sight relative to certain elements (Jenkins 2009; Yao et al. 2009; Whittet 2010), together with observations of molecular features in other wavelength bands. An example of a potentially detectable signature of such material is the K resonance of the CO molecule expected at a rest wavelength of  $23.21 \text{ \AA}$

(Barrus et al. 1979). This line is separated from the nearest feature we clearly detect by approximately  $100 \text{ m}\text{\AA}$ , which can be compared with the magnitude of the wavelength shifts we adopt in order to get acceptable fits, the largest of which is  $33 \text{ m}\text{\AA}$ . Therefore, we conclude that the existing atomic absorption data are not sufficiently uncertain to mask the presence of this molecular signature. The search for molecular and solid features in X-ray spectra remains of great interest, both as tests of the atomic data and of the models for the ISM.

We believe that the present benchmark has produced an improved version of the `warmabs` model which can now be used for a more extensive and reliable study of oxygen K photoabsorption towards other X-ray sources. This will be the next step of the current study where the oxygen abundance variations in the ISM are certainly of interest. In a similar fashion, we also intend to evaluate the Ne and Fe edge regions for ongoing physical model refinement.

Part of this work was carried out by Efraín Gatuuz during attendance in July 2011 to the Committee On Space Research (COSPAR) Capacity Building Workshop in San Juan, Argentina, and visits in August 2011 to the Laboratory of High Energy Astrophysics, NASA Goddard Space Flight Center, Greenbelt, Maryland, USA, and in February–March 2012 to the European Space Astronomy Centre (ESAC), Madrid, Spain, the latter funded by the COSPAR Fellowship Program. Warm hospitality and tutelage at these institutions are kindly acknowledged, in particular from Andy Pollock and Carlos Gabriel at ESAC. We would also like to thank Michael Nowak from MIT for useful discussions relating the pileup model and the ISIS implementation.

## REFERENCES

- Asplund, M., Grevesse, N., Sauval, A. J., Allende Prieto, C., & Kiselman, D. 2004, *A&A*, 417, 751
- Asplund, M., Grevesse, N., Sauval, A. J., & Scott, P. 2009, *ARA&A*, 47, 481
- Badnell, N. R. 1986, *J. Phys. B: At. Mol. Opt. Phys.*, 19, 3827
- . 1997, *J. Phys. B: At. Mol. Opt. Phys.*, 30, 1
- Barrus, D. M., Blake, R. L., Burek, A. J., Chambers, K. C., & Pregonzer, A. L. 1979, *Phys. Rev. A*, 20, 1045
- Baumgartner, W. H., & Mushotzky, R. F. 2006, *ApJ*, 639, 929
- Bautista, M. A., & Kallman, T. R. 2001, *ApJS*, 134, 139
- Behar, E., & Netzer, H. 2002, *ApJ*, 570, 165
- Berrington, K. A., Burke, P. G., Butler, K., Seaton, M. J., Storey, P. J., Taylor, K. T., & Yan, Y. 1987, *J. Phys. B: At. Mol. Opt. Phys.*, 20, 6379
- Cackett, E. M., et al. 2008, *ApJ*, 674, 415
- Costantini, E., et al. 2012, *A&A*, 539, A32
- Cowan, R. D. 1981, *The theory of atomic structure and spectra* (Berkeley, CA: Univ. of California Press)
- D’Avanzo, P., et al. 2006, *The Astronomer’s Telegram*, 724, 1
- Dickey, J. M., & Lockman, F. J. 1990, *ARA&A*, 28, 215
- Eissner, W., Jones, M., & Nussbaumer, H. 1974, *Computer Physics Communications*, 8, 270

- García, J., Mendoza, C., Bautista, M. A., Gorczyca, T. W., Kallman, T. R., & Palmeri, P. 2005, *ApJS*, 158, 68
- García, J., Ramírez, J. M., Kallman, T. R., Witthoeft, M., Bautista, M. A., Mendoza, C., Palmeri, P., & Quinet, P. 2011, *ApJ*, 731, L15
- Gierliński, M., Done, C., & Page, K. 2008, *MNRAS*, 388, 753
- . 2009, *MNRAS*, 392, 1106
- Gorczyca, T. W., & McLaughlin, B. M. 2000, *J. Phys. B: At. Mol. Opt. Phys.*, 33, L859
- Gorczyca, T. W., & Robicheaux, F. 1999, *Phys. Rev. A*, 60, 1216
- Grevesse, N., & Sauval, A. J. 1998, *Space Sci. Rev.*, 85, 161
- Gu, M. F., Schmidt, M., Beiersdorfer, P., Chen, H., Thorn, D. B., Träbert, E., Behar, E., & Kahn, S. M. 2005, *ApJ*, 627, 1066
- Hanke, M., Wilms, J., Nowak, M. A., Pottschmidt, K., Schulz, N. S., & Lee, J. C. 2009, *ApJ*, 690, 330
- Jenkins, E. B. 2009, *ApJ*, 700, 1299
- Juett, A. M., Schulz, N. S., & Chakrabarty, D. 2004, *ApJ*, 612, 308
- Kalberla, P. M. W., Burton, W. B., Hartmann, D., Arnal, E. M., Bajaja, E., Morras, R., & Pöppel, W. G. L. 2005, *A&A*, 440, 775
- Kallman, T., & Bautista, M. 2001, *ApJS*, 133, 221
- Kallman, T. R., Bautista, M. A., Goriely, S., Mendoza, C., Miller, J. M., Palmeri, P., Quinet, P., & Raymond, J. 2009, *ApJ*, 701, 865

- Kallman, T. R., Palmeri, P., Bautista, M. A., Mendoza, C., & Krolik, J. H. 2004, *ApJS*, 155, 675
- Liu, Q. Z., van Paradijs, J., & van den Heuvel, E. P. J. 2007, *A&A*, 469, 807
- Miller, J. M., Homan, J., Steeghs, D., & Wijnands, R. 2006a, *The Astronomer's Telegram*, 746, 1
- Miller, J. M., et al. 2006b, *ApJ*, 646, 394
- Palmeri, P., Quinet, P., Mendoza, C., Bautista, M. A., García, J., Witthoeft, M. C., & Kallman, T. R. 2012, *A&A*, 543, A44
- Pinto, C., Kaastra, J. S., Costantini, E., & Verbunt, F. 2010, *A&A*, 521, A79
- Pradhan, A. K., Chen, G. X., Delahaye, F., Nahar, S. N., & Oelgoetz, J. 2003, *MNRAS*, 341, 1268
- Remillard, R., Levine, A. M., Morgan, E. H., Markwardt, C. B., & Swank, J. H. 2006, *The Astronomer's Telegram*, 714, 1
- Roy, J., Agrawal, P. C., Paul, B., & Duorah, K. 2011, *MNRAS*, 412, 1011
- Rupen, M. P., Dhawan, V., & Mioduszewski, A. J. 2006, *The Astronomer's Telegram*, 721, 1
- Rykoff, E. S., Miller, J. M., Steeghs, D., & Torres, M. A. P. 2007, *ApJ*, 666, 1129
- Sala, G., Greiner, J., Bottacini, E., & Haberl, F. 2007, *Ap&SS*, 309, 315
- Savage, B. D., et al. 2003, *ApJS*, 146, 125
- Schmidt, M., Beiersdorfer, P., Chen, H., Thorn, D. B., Träbert, E., & Behar, E. 2004, *ApJ*, 604, 562

- Scott, N. S., & Burke, P. G. 1980, *J. Phys. B: At. Mol. Opt. Phys.*, 13, 4299
- Scott, N. S., & Taylor, K. T. 1982, *Computer Physics Communications*, 25, 347
- Seaton, M. 1987, *J. Phys. B: At. Mol. Opt. Phys.*, 20, 6363
- Stasińska, G., et al. 2012, in *EAS Publications Series*, Vol. 54, *EAS Publications Series*, ed. G. Stasińska, N. Prantzos, G. Meynet, S. Simón-Díaz, C. Chiappini, M. Dessauges-Zavadsky, C. Charbonnel, H.-G. Ludwig, C. Mendoza, N. Grevesse, M. Arnould, B. Barbuy, Y. Lebreton, A. Decourchelle, V. Hill, P. Ferrando, G. Hébrard, F. Durrel, M. Katsuma, & C. J. Zeippen, 65–186
- Stolte, W. C., et al. 1997, *Journal of Physics B Atomic Molecular Physics*, 30, 4489
- Torres, M. A. P., Steeghs, D., Jonker, P. G., Luhman, K., McClintock, J. E., & Garcia, M. R. 2006, *The Astronomer’s Telegram*, 733, 1
- Verner, D. A., Ferland, G. J., Korista, K. T., & Yakovlev, D. G. 1996, *ApJ*, 465, 487
- Whittet, D. C. B. 2010, *ApJ*, 710, 1009
- Wilms, J., Allen, A., & McCray, R. 2000, *ApJ*, 542, 914
- Yao, Y., Schulz, N. S., Gu, M. F., Nowak, M. A., & Canizares, C. R. 2009, *ApJ*, 696, 1418
- Yao, Y., & Wang, Q. D. 2006, *ApJ*, 641, 930

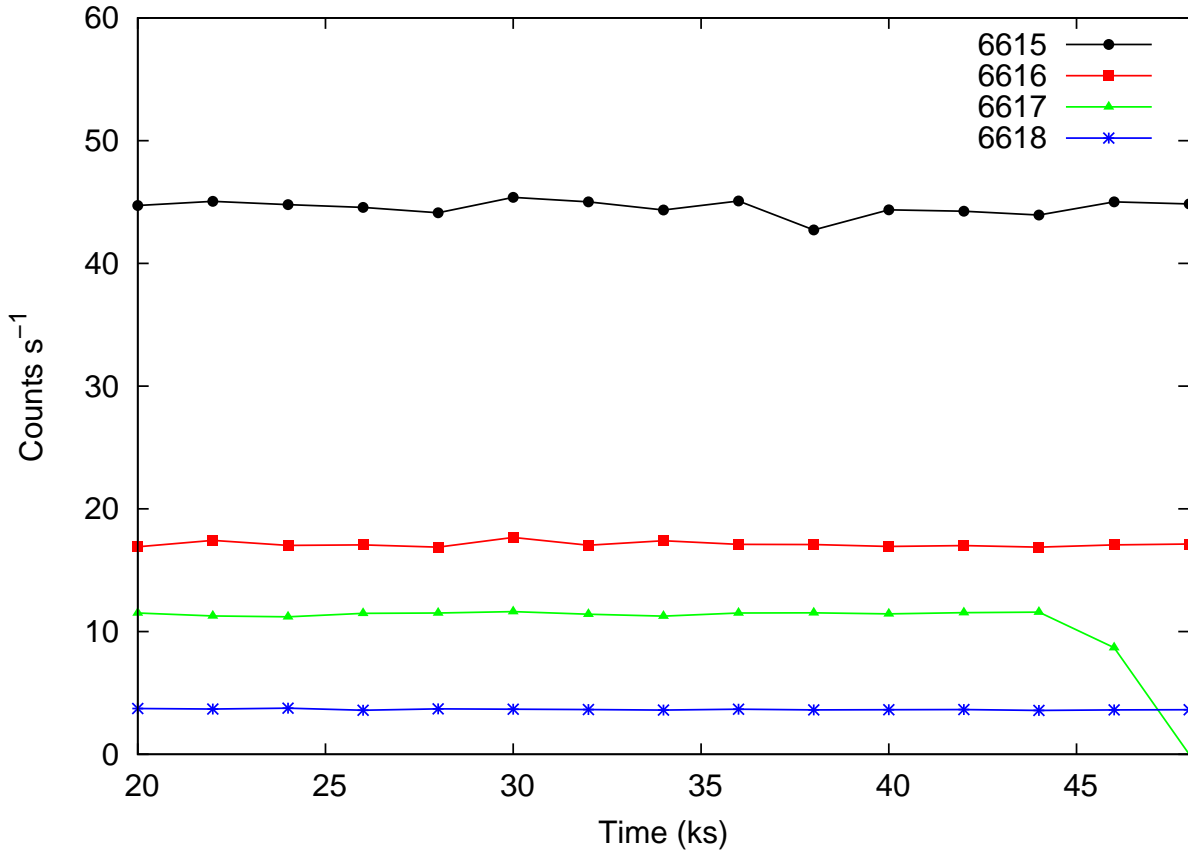


Fig. 1.— Light curves of the four observations, ObsID 6615, 6616, 6617, and 6618, in units of counts/s. The approximately constant average counts/s that prevails is an indication of a low variability degree.

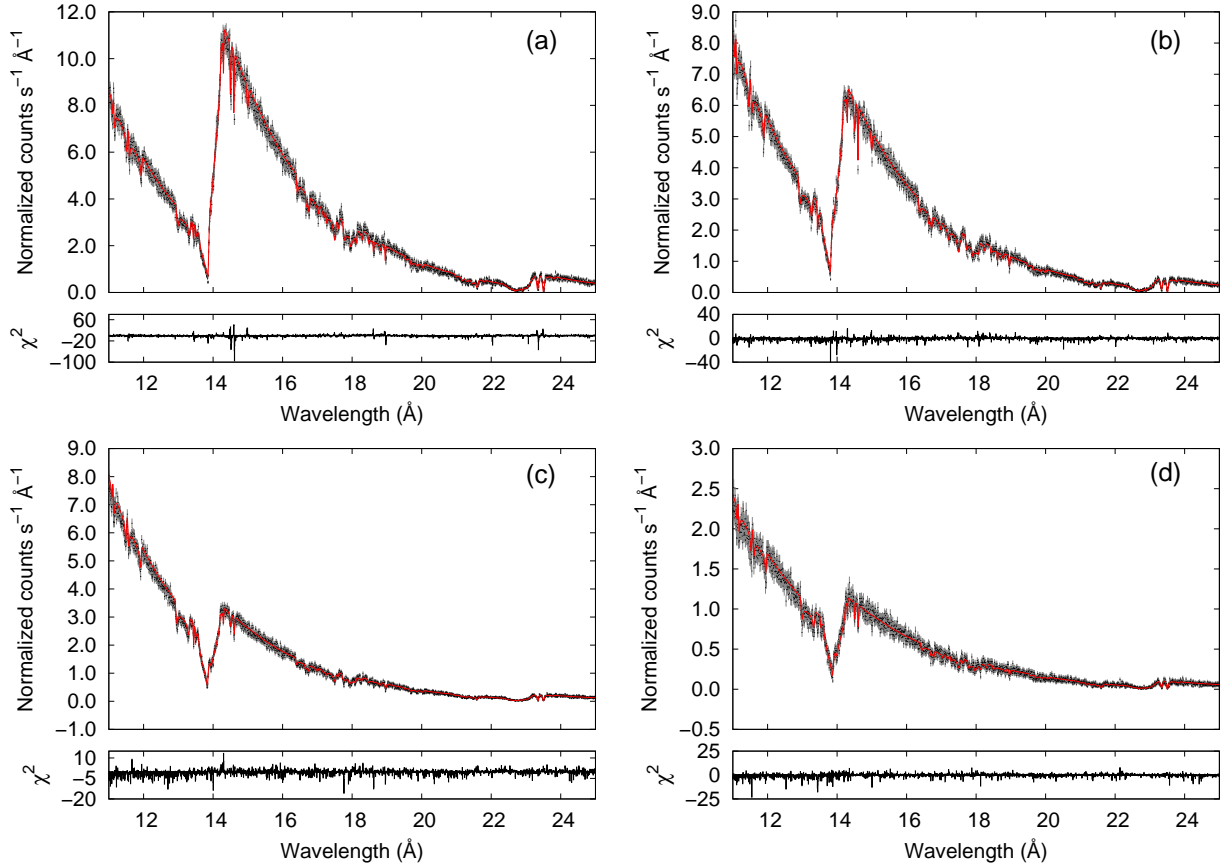


Fig. 2.— *Chandra* MEG spectra of the X-ray binary XTE J1817-330 simultaneously fitted in the 11–25 Å region using the TBnew model. (a) ObsID 6615. (b) ObsID 6616. (c) ObsID 6617. (d) ObsID 6618. See Table 2 for further details pertaining to these observations. In each panel, the black data points are the observations while the solid red lines correspond to the best-fit models. Residuals are shown as histograms for each case in units of  $\chi^2$ . Note the large residuals in the oxygen K-edge region, particularly in the neighborhood of the O I and O II  $K\alpha$  lines at  $\approx 23.50$  Å and  $\approx 23.35$  Å, respectively.

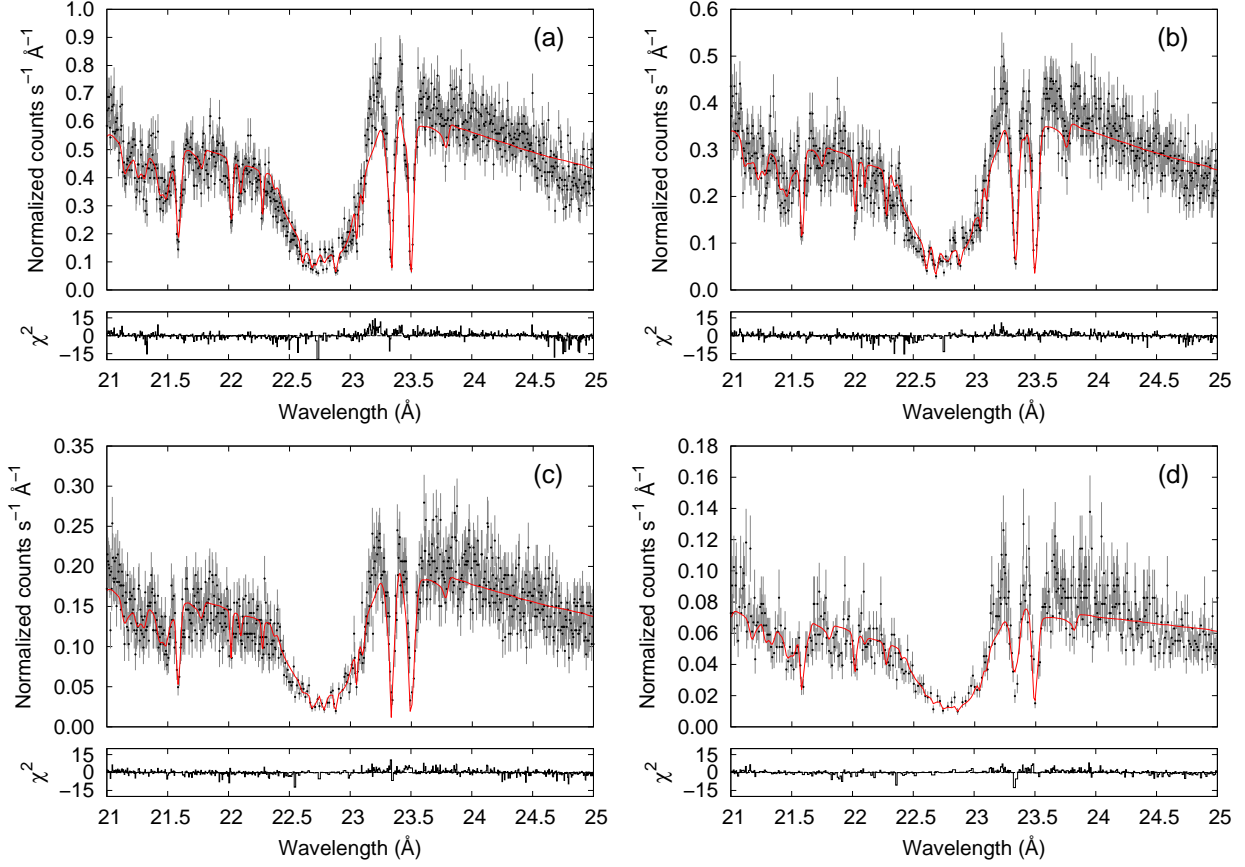


Fig. 3.— Spectral fit of the *Chandra* MEG observations of XTE J1817-330 in the oxygen absorption region (21–25 Å) using a simple functional model (power law and several Gaussian profiles). (a) ObsID 6615. (b) ObsID 6616. (c) ObsID 6617. (d) ObsID 6618. The observed absorption features are interpreted as: the neutral O K-edge ( $\approx 23.1$  Å); the  $K\alpha$ ,  $K\beta$ , and  $K\gamma$  lines of O I ( $\approx 23.50$  Å,  $\approx 22.88$  Å, and  $\approx 22.68$  Å, respectively); the  $K\alpha$ ,  $K\beta$ , and  $K\gamma$  lines of O II ( $\approx 23.35$  Å,  $\approx 22.28$  Å, and  $\approx 22.10$  Å, respectively); and the  $K\alpha$  lines of O III, O VI, and O VII ( $\approx 23.10$  Å,  $\approx 22.02$  Å, and  $\approx 21.58$  Å, respectively). See Table 4 for more details.

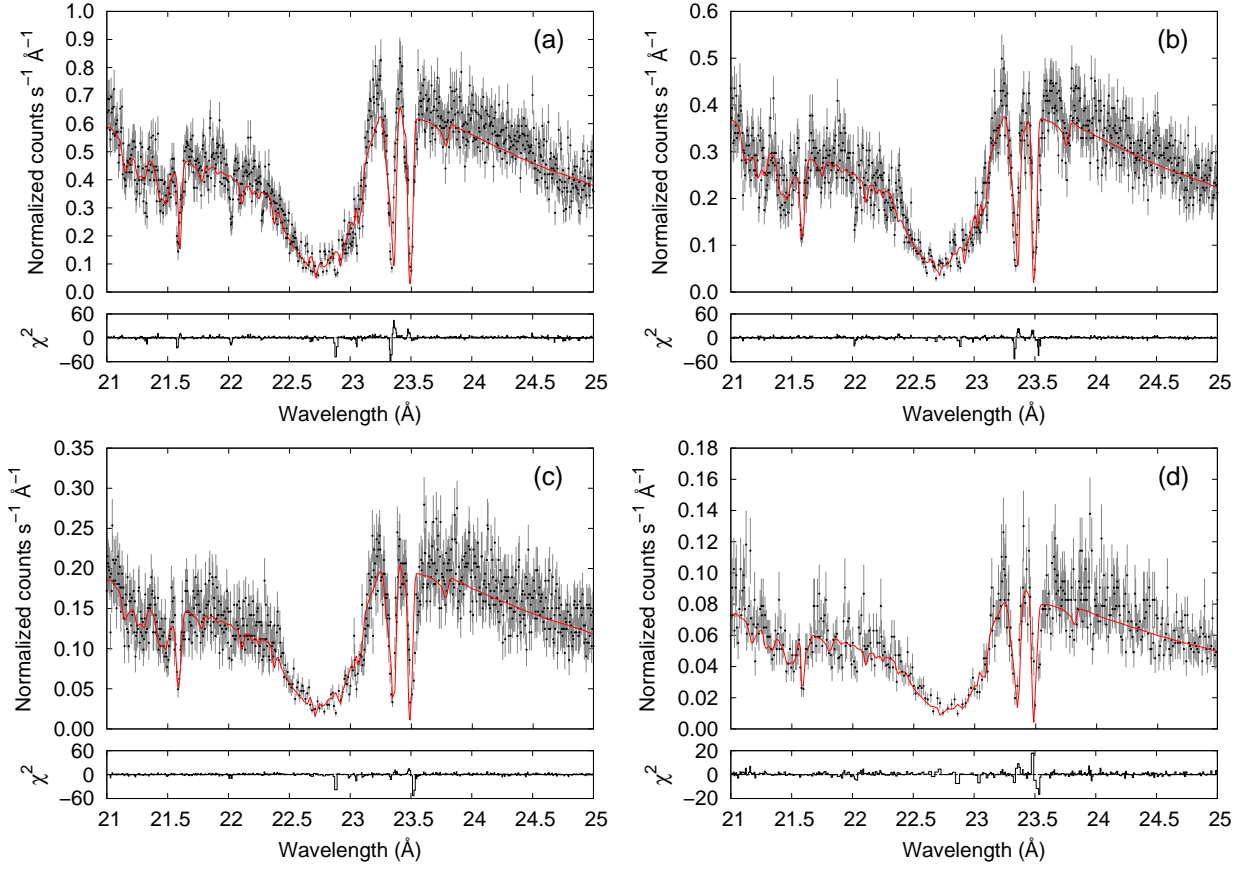


Fig. 4.— Spectral fit of the *Chandra* MEG observations of XTE J1817-330 in the oxygen absorption region (21–25 Å) using a `powerlaw*warmabs` physical model. (a) ObsID 6615. (b) ObsID 6616. (c) ObsID 6617.(d) ObsID 6618.

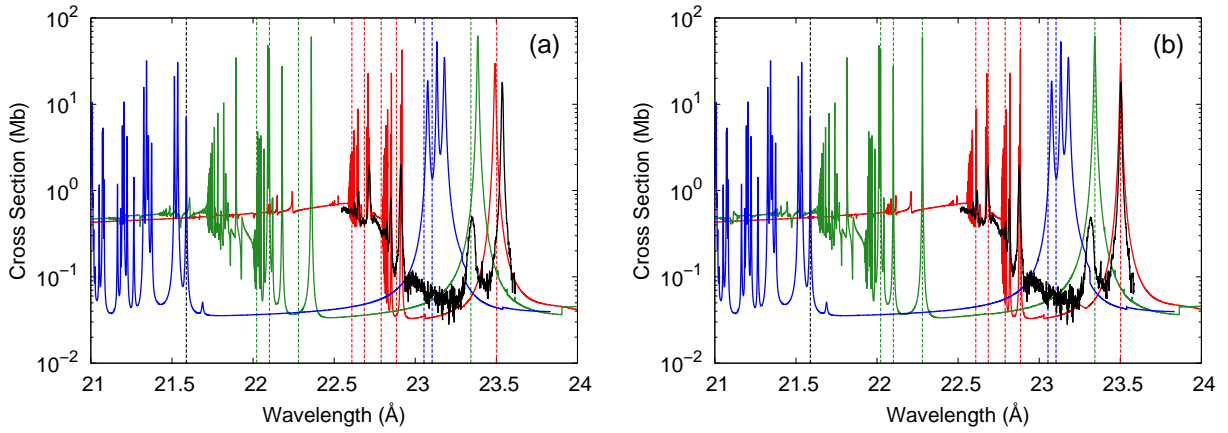


Fig. 5.— Comparison of the theoretical photoabsorption cross sections for O I (red), O II (green), and O III (blue) computed by García et al. (2005) which are implemented in the `warmabs` model. The black solid line is the laboratory measurement by Stolte et al. (1997) showing peaks of O I and O<sub>2</sub>. The vertical dashed lines are placed at the wavelengths of the observed absorption lines (see Table 4). Panel (a) displays the original cross sections while panel (b) shows the same curves after the wavelength shifts are applied to both O I and O II (see text for details).

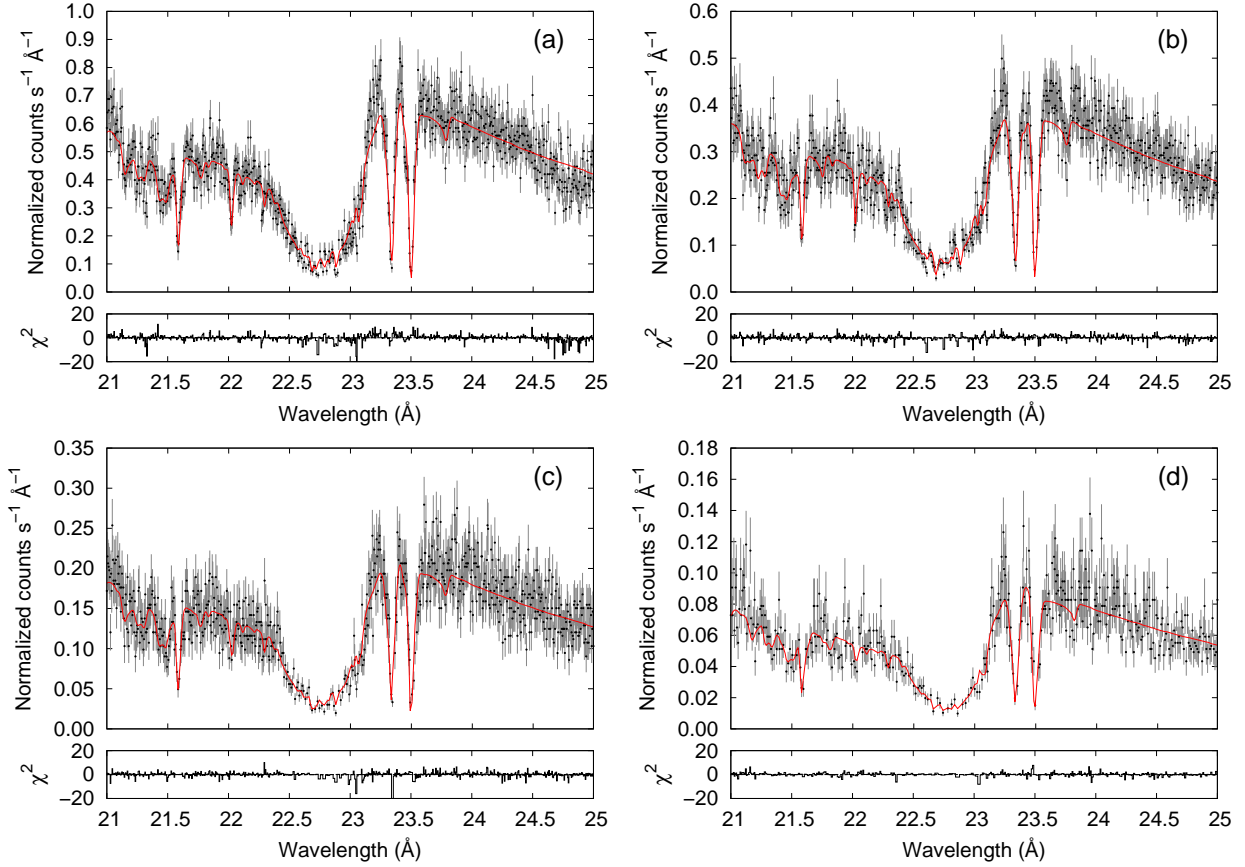


Fig. 6.— Spectral fit of the *Chandra* MEG observations of XTE J1817-330 in the oxygen absorption region (21–25 Å) using a `powerlaw*warmabs` physical model, after the wavelength corrections in the O I and O II atomic cross sections are introduced. (a) ObsID 6615. (b) ObsID 6616. (c) ObsID 6617. (d) ObsID 6618.

Table 1. Comparison of EBIT and theoretical wavelengths ( $\text{\AA}$ ) for K lines

Ion	Lower level ( $J$ )	Upper level ( $J'$ )	EBIT	Theory
O VI	$1s^2 2s(1/2)$	$1s 2s 2p(1/2, 3/2)$	$22.0194 \pm 0.0016^a$	$22.00^c$
			$22.374 \pm 0.008^b$	$22.05^d$
				$22.03^e$
O V	$1s^2 2s^2(0)$	$1s 2s^2 2p(1)$	$22.374 \pm 0.003^a$	$22.33^c$
			$22.370 \pm 0.010^b$	$22.35^d$
				$22.37^e$
O IV	$1s^2 2s^2 2p(1/2, 3/2)$	$1s 2s^2 2p^2(1/2, 3/2)$	$22.741 \pm 0.005^b$	$22.78^c$
				$22.73^d$
				$22.75^e$
O III	$1s^2 2s^2 2p^2(1, 2)$	$1s 2s^2 2p^3(1)$	$22.071 \pm 0.006^b$	$23.08^c$
				$23.05^d$
				$23.07^e$

<sup>a</sup>EBIT measurement (Schmidt et al. 2004)

<sup>b</sup>EBIT measurement (Gu et al. 2005)

<sup>c</sup>HULLAC calculation (Behar & Netzer 2002)

<sup>d</sup> $R$ -matrix calculation (Pradhan et al. 2003)

<sup>e</sup>HFR calculation (García et al. 2005)

Table 2. *Chandra* observations used in this paper

ObsID	Date	Exposure (ks)	Instrument	Grating	Label
6615	2006 Feb 13	18	HETG-ACIS	MEG	Observation 1
6616	2006 Feb 24	29	HETG-ACIS	MEG	Observation 2
6617	2006 Mar 15	47	HETG-ACIS	MEG	Observation 3
6618	2006 May 22	51	HETG-ACIS	MEG	Observation 4

Table 3. Broadband simultaneous fit parameters

Model	Parameter	Value
TBNew	$N_{\text{H}}$ ( $10^{21}$ cm $^{-2}$ )	$1.66^{+0.03}_{-0.04}$
TBNew	Neon abundance ( $A_{\text{Ne}}$ )	$2.258 \pm 0.080$
TBNew	Iron abundance ( $A_{\text{Fe}}$ )	$1.302 \pm 0.050$
TBNew	Oxygen abundance ( $A_{\text{O}}$ )	$1.178 \pm 0.022$
Power-law	Normalization	$9.416 \pm 0.064^a$
		$7.039 \pm 0.041^b$
		$4.613 \pm 0.042^c$
		$1.481 \pm 0.001^d$
Power-law	Photon Index	$1.545 \pm 0.030^a$
		$1.618 \pm 0.030^b$
		$1.735 \pm 0.029^c$
		$2.242 \pm 0.038^d$
SimpleGpile2	$\beta$	$0.050 \pm 0.001^a$
		$0.051 \pm 0.001^b$
		$0.050 \pm 0.001^c$
		$0.049 \pm 0.001^d$
Reduced chi-square	$\chi^2$	1.208

Note. — Abundances relative to the solar values of Wilms et al. (2000).

<sup>a</sup>ObsID 6615

<sup>b</sup>ObsID 6616

<sup>c</sup>ObsID 6617

<sup>d</sup>ObsID 6618

Table 4. Absorption line assignments

Ion	Transition	$\lambda^a$ (Å)	$\lambda^b$ (Å)
O VII	$1s^2 \ ^1S - [1s]2p \ ^1P^o$	$21.589 \pm 0.003$	$21.60 \pm 0.06$
O VI	$2s \ ^2S - [1s]2s2p \ ^2P^o$	$22.022 \pm 0.003$	
O II	$2p^3 \ ^4S^o - [1s]2p^34p \ ^4P$	$22.101 \pm 0.005$	
O II	$2p^3 \ ^4S^o - [1s]2p^33p \ ^4P$	$22.280 \pm 0.003$	
O I	$2p^4 \ ^3P - [1s]2p^4(^2P)4p \ ^3P^o$	$22.609 \pm 0.007$	
O I	$2p^4 \ ^3P - [1s]2p^4(^2P)3p \ ^3P^o$	$22.686 \pm 0.004$	
O I	$2p^4 \ ^3P - [1s]2p^4(^4P)4p \ ^3P^o$	$22.790 \pm 0.001$	
O I	$2p^4 \ ^3P - [1s]2p^4(^4P)3p \ ^3P^o$	$22.884 \pm 0.004$	$22.91 \pm 0.03$
O III	$2p^2 \ ^3P - [1s]2p^3 \ ^3P^o$	$23.054 \pm 0.001$	$23.13 \pm 0.09$
O III	$2p^2 \ ^3P - [1s]2p^3 \ ^3D^o, \ ^3S^o$	$23.104 \pm 0.005$	$23.13 \pm 0.09$
O II	$2p^3 \ ^4S^o - [1s]2p^4 \ ^4P$	$23.358 \pm 0.002$	$23.35 \pm 0.03$
O I	$2p^4 \ ^3P - [1s]2p^5 \ ^3P^o$	$23.502 \pm 0.001$	$23.52 \pm 0.02$

<sup>a</sup>Present work

<sup>b</sup>Sala et al. (2007)

Table 5. `warmabs` simultaneous fit parameters

Model	Parameter	Value
Warmabs	$N_{\text{H}}$ ( $10^{21}$ cm $^{-2}$ )	$1.38 \pm 0.01$
Warmabs	Log ionization parameter ( $\log \xi$ )	$-2.699 \pm 0.023$
Warmabs	Oxygen abundance ( $A_{\text{O}}$ )	$0.689^{+0.015}_{-0.010}$
Power-law	Normalization	$2.384^a$
		$2.544^b$
		$1.511^c$
		$0.685^d$
Power-law	Photon Index	$3.044^a$
		$2.479^b$
		$2.720^c$
		$2.617^d$
Reduced chi-square	$\chi^2$	1.245

Note. — Oxygen abundance relative to the solar value of Grevesse & Sauval (1998).

<sup>a</sup>ObsID 6615

<sup>b</sup>ObsID 6616

<sup>c</sup>ObsID 6617

<sup>d</sup>ObsID 6618

Table 6. Hydrogen column density comparison

Method	$N_H$ ( $10^{21}$ cm $^{-2}$ )
<b>TBnew fit<sup>a</sup></b>	$1.66^{+0.03}_{-0.04}$
<b>warmabs fit<sup>a</sup></b>	$1.38 \pm 0.1$
21 cm survey <sup>b</sup>	1.58
21 cm survey <sup>c</sup>	1.39
Spectral model fit <sup>d</sup>	$1.55 \pm 0.05$
Spectral model fit <sup>e</sup>	1.2
Spectral model fit <sup>f</sup>	$0.88 - 0.97$
Spectral model fit <sup>g</sup>	$1.0 - 3.0$
Spectral model fit <sup>h</sup>	$1.08 \pm 0.05$

<sup>a</sup>Present work

<sup>b</sup>Dickey & Lockman (1990)

<sup>c</sup>Kalberla et al. (2005)

<sup>d</sup>Sala et al. (2007)

<sup>e</sup>Rykoff et al. (2007), Gierliński et al. (2008), Roy et al. (2011)

<sup>f</sup>Miller et al. (2006a)

<sup>g</sup>Torres et al. (2006)

<sup>h</sup>Gierliński et al. (2009)

Table 7. Equivalent widths comparison for the oxygen  $K\alpha$  transitions in the ISM

Source	O I $K\alpha$ (mÅ)	O II $K\alpha$ (mÅ)	O III $K\alpha$ (mÅ)	O VI $K\alpha$ (mÅ)	O VII $K\alpha$ (mÅ)
XTE J1817-330 <sup>a</sup>	51 ± 5	52 ± 5	16 ± 5	14 ± 5	54 ± 4
XTE J1817-330 <sup>b</sup>	70 ± 20	40 ± 20	30 ± 30		40 ± 30
Cyg X-2 <sup>c</sup>	67±11	26±17	9±8		
Cyg X-2 <sup>d</sup>	50 ± 3	28 ± 6		11 ± 2	
4U 1543-624 <sup>c</sup>	68±11	41±11	18±5		
4U 1820-30 <sup>c</sup>	70±20	41±17	20±10		
4U 1735-44 <sup>c</sup>	80±30	40±20	24±10		
GX 9+9 <sup>c</sup>	80±30	50±19	27±13		
4U 1636-53 <sup>c</sup>	90±30	60±20	33±13		
Cyg X-1 (ObsID 3407) <sup>c</sup>	95±17	20±11	35±15		

<sup>a</sup>Present work

<sup>b</sup>Sala et al. (2007)

<sup>c</sup>Juett et al. (2004)

<sup>d</sup>Yao et al. (2009)

Table 8. Oxygen column density comparison

Source	O I ( $10^{17} \text{ cm}^{-2}$ )	O II ( $10^{17} \text{ cm}^{-2}$ )	O III ( $10^{17} \text{ cm}^{-2}$ )	O VI ( $10^{15} \text{ cm}^{-2}$ )	O VII ( $10^{15} \text{ cm}^{-2}$ )
XTE J1817-330 <sup>a</sup>	$3.18 \pm 0.79$	$2.18 \pm 0.54$	$0.35 \pm 0.08$	$5.06 \pm 2.53$ <sup>d</sup> $5.99 \pm 1.9$ <sup>e</sup> $71.12 \pm 29.15$ <sup>f</sup>	$45 \pm 18$ <sup>d</sup> $988 \pm 405$ <sup>e</sup> $4484 \pm 1838$ <sup>f</sup>
XTE J1817-330 <sup>b</sup>	$5.85 \pm 1.75$	$0.49 \pm 0.12$	$0.07 \pm 0.02$		
PG 1302-102 <sup>c</sup>				$0.16 \pm 0.03$	
Mrk 1383 <sup>c</sup>				$0.38 \pm 0.07$	
ESO 141-G55 <sup>c</sup>				$0.31 \pm 0.06$	
PKS 2005-489 <sup>c</sup>				$0.60 \pm 0.01$	

<sup>a</sup>Calculated from the EWs and the curves of growth (see section 7 ).

<sup>b</sup>Derivated from the `warmabs` model fit using the solar value of Grevesse & Sauval (1998) (see section 5)

<sup>c</sup>Obtained from FUSE data by Savage et al. (2003)

<sup>d</sup>Using a velocity dispersion  $v = 200 \text{ km/s}$

<sup>e</sup>Using a velocity dispersion  $v = 100 \text{ km/s}$

<sup>f</sup>Using a velocity dispersion  $v = 20 \text{ km/s}$